Supplemental Material (SM) for: "Emergent Polar Metal Phase in a Van der Waals Mott Magnet"

Shiyu Deng,[1,2] Matthew J. Coak,[3] Charles R. S. Haines,[4] Hayrullo Hamidov,[1,5] Giulio I. Lampronti,[6] David M. Jarvis,[1,2] Xiaotian Zhang,[1] Cheng Liu,[1] Dominik Daisenberger,[7] Mark R. Warren,[7] Thomas C Hansen,[2] Stefan Klotz,[8] Chaebin Kim,[9] Pengtao Yang,[10,11] Bosen Wang,[10,11] Jinguang Cheng,[10,11] Je-Geun Park,[9] Andrew R. Wildes,[2] and Siddharth S Saxena[1,12]

[1] *Cavendish Laboratory, University of Cambridge, J.J. Thomson Avenue, Cambridge, CB3 0HE, UK*
[2] *Institut Laue-Langevin, 71 Avenue des Martyrs, 38000 Grenoble, France*
[3] *School of Physics and Astronomy, University of Birmingham, Edgbaston, Birmingham B15 2TT, United Kingdom*
[4] *Physics, University of East Anglia, Norwich NR4 7TJ, United Kingdom*
[5] *Navoi State University of Mining and Technologies, 72 M. Tarobiy Street, Navoi 210100, Uzbekistan*
[6] *Department of Earth Sciences, University of Cambridge, Downing Street, Cambridge CB2 3EQ, United Kingdom*
[7] *Diamond Light Source, Harwell Science and Innovation Campus, Didcot, OX11 0DE, United Kingdom*
[8] *Sorbonne Universite, IMPMC, CNRS, UMR 7590, 4 Place Jussieu, 75252 Paris, France*
[9] *Department of Physics and Astronomy, Seoul National University, Seoul 08826, Republic of Korea*
[10] *Beijing National Laboratory for Condensed Matter Physics and Institute of Physics, Chinese Academy of Sciences, Beijing 100190, China*
[11] *School of Physical Sciences, University of Chinese Academy of Sciences, Beijing 100190, China*
[12] *British Management University Tashkent, 35 Mirza Bobur Street, Tashkent, Uzbekistan*

I. SYNCHROTRON DIFFRACTION AND CRYSTALLINE STRUCTURES

A. Experiment Configuration

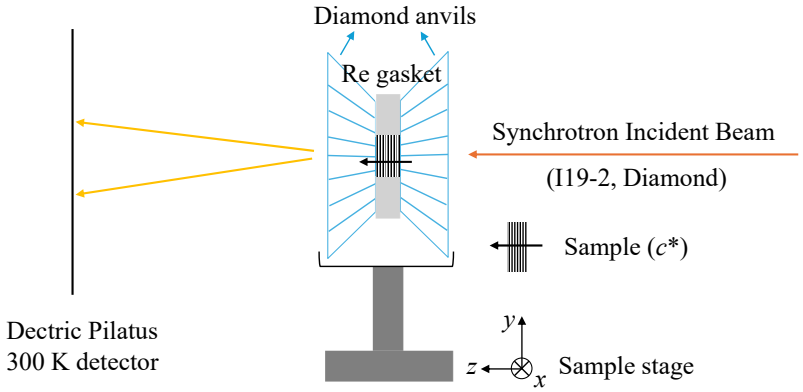

FIG. 1. Schematic display of the experimental setup of one Diamond Anvil Cell (DAC) loaded with $FePSe_3$ single-crystal samples on the I19-2 beamline.

Fig. 1 shows the schematic experimental setup for the synchrotron experiments. Powder diffraction measurements were performed on I15 and single crystal experiments on I19-2 (I19, Experimental hutch 2). Diamond anvil cells were used for both with the incident beam initially aligned along the anvil axis. The detector was positioned after the sample. A MAR345 area detector was used on I15 and a Dectric Pilatus 300 K detector was used on I19-2.

The sample was not moved for the powder measurements, and data were collected as a function of applied pressure. For the single crystal measurements, the c^* axis is normal to the plate-like sample and was approximately parallel to the anvil axis. The cell was rotated around the vertical axis on the instrument, labelled as the y-axis in Fig. 1. The data therefore provided a reciprocal space map, limited by the opening angles of the diamond anvil cell.

B. Pressure Determination and Calibration

To determine the pressure inside the DAC, a pressure gauge must also be put into the sample chamber, as close to the sample as possible. We inserted several spheres of ruby with approximately 10 μm diameter into the sample chamber. The fluorescence spectrum of the ruby was measured using an exciting optical laser and a spectrometer. The wavelength of the $R1$ fluorescence line shits to higher values, indicating the increased pressure P according to Eq. 1 [1, 2]:

$$P = \frac{A}{B}\left\{\left[\frac{\lambda}{\lambda_0}\right]^B - 1\right\} \tag{1}$$

where $A = 248.4$ GPa, $B = 7.665$ for hydrostatic pressures. λ_0 is the $R1$ peak's corresponding wavelength at ambient pressure and room temperature. We measured the value of λ_0 before closing each DAC cell as a calibration. Then we applied constant load to the membrane of a DAC cell while tracking the $R1$ peak position. Each time after increasing the load, we waited for about 5 minutes so that the pressure inside the sample space could be better stabilised. Then, λ was measured to calculate the pressure using Eq. 1 before and after the data collection. Fig. 2 shows the recorded load and the calculated pressure values for the two DACs loaded with $FePSe_3$ powder samples, with and without the pressure-transmitting medium helium. The average of pressure values before and after the data collection is plotted, with the deviation size being the error bar at each point. It can be seen that the real error bar size is rather small, which suggested that the pressure inside the cell during the data collection was stable and reliable.

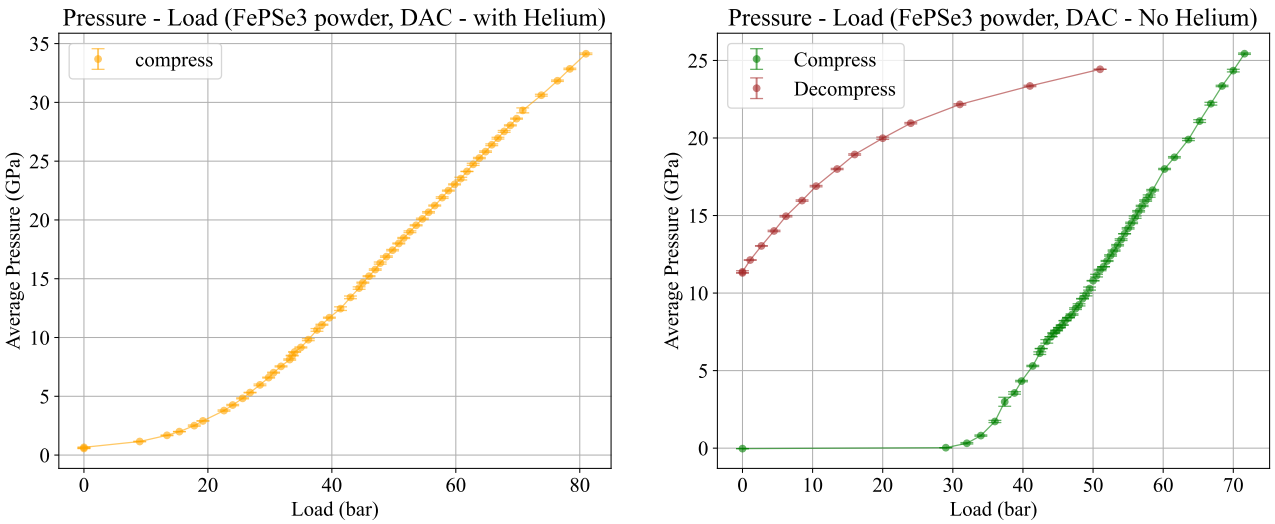

FIG. 2. The calculated pressure values from the Ruby spectrum as a function of the applied constant load on the membrane of a DAC for $FePSe_3$ powder samples with (only compression) and without (both compression and de-compression) helium as a pressure-transmitting medium.

C. Powder Samples in a DAC

1. *Sample Averaging*

A characteristic powder diffraction pattern of $FePSe_3$ in the diamond anvil cell is shown in Fig. 3. The powder diffraction rings are clearly visible and their intensities are reasonably homogeneous as a function of the azimuthal angle, establishing that the scattering was effectively free of preferred orientation. Bright spots from the diamond anvils are also present and were removed in the data reduction.

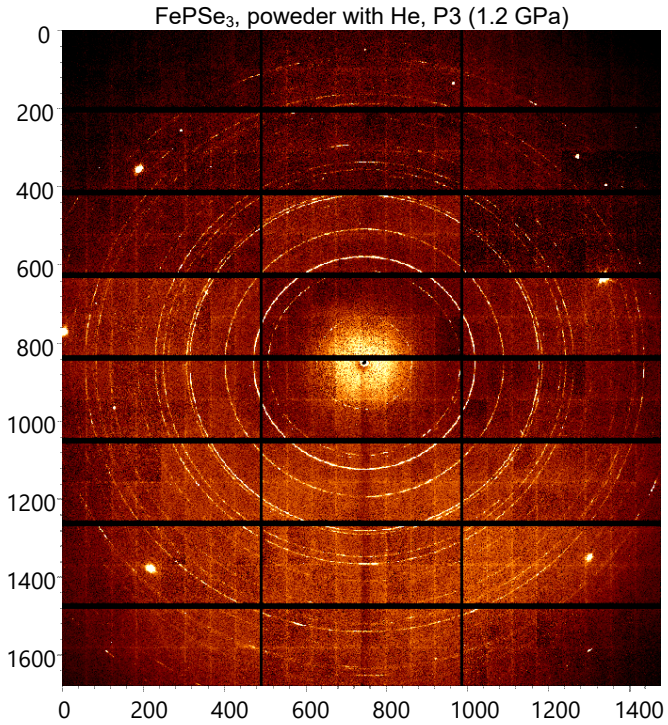

FIG. 3. Original diffraction patterns of $FePSe_3$ powder sample loaded with helium as a PTM in one DAC at 1.2 GPa. The sparkling points are peaks from the diamond.

2. Data Processing and Background Subtraction

We used DAWN − II [3] to analyze data. At each pressure, the centre of the powder rings had to be determined carefully. The intensity was integrated over the rings with the radius being converted into 2θ or d spacing. Fig. 4 provides examples of the resulting intensity in the 2θ space at two characteristic pressures before and after the c collapse. The observed integrated intensity is shown as blue crosses.

Afterward, we used GSAS − II [4] to perform Rietveld refinement to determine the crystal structure. The calculated peak intensity is shown in green in Fig. 4. The simulated peak positions for $FePSe_3$ and rhenium are also denoted with solid lines on the plot. As the sample space shrinks with increased pressure, the beam impinges on the rhenium gasket.

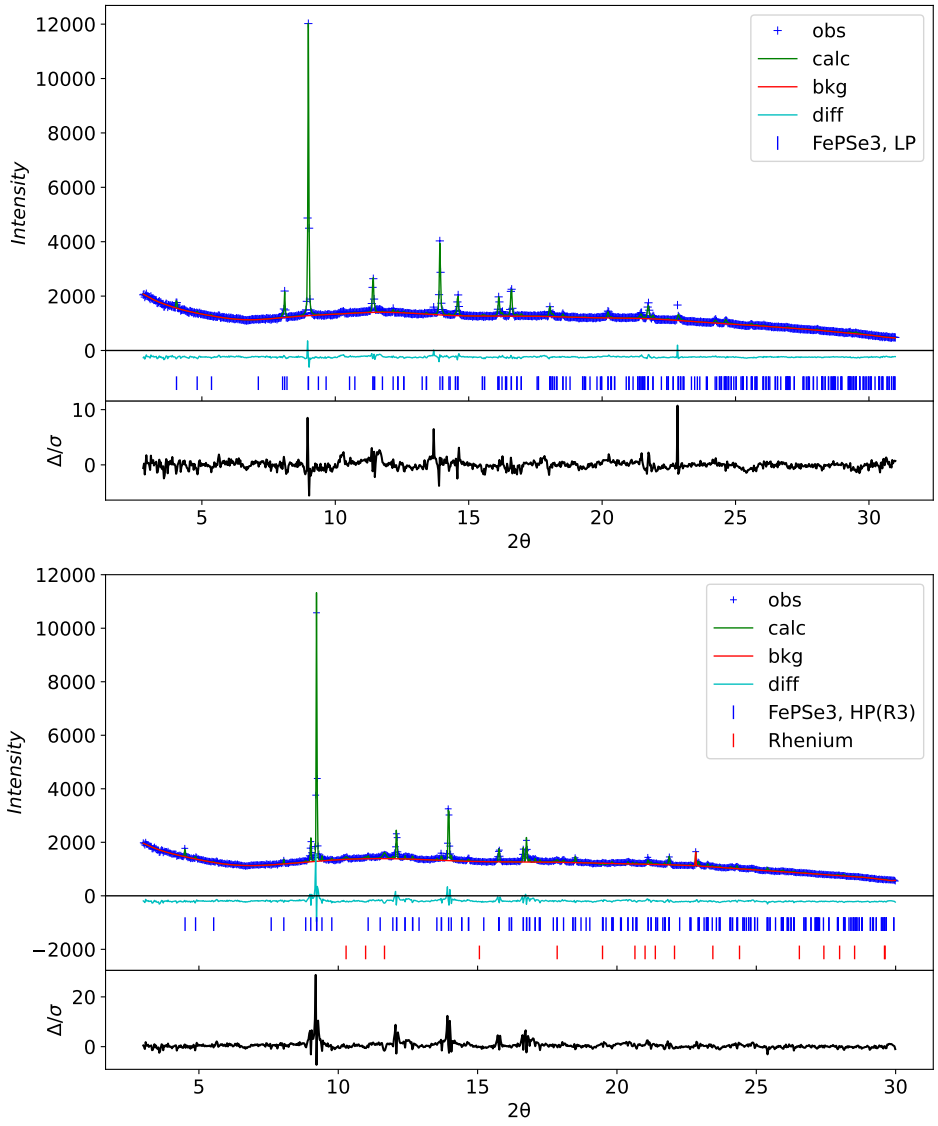

FIG. 4. (a) The integrated powder diffraction intensity data of $FePSe_3$ at 7.5 and 8.1 GPa (blue), using the LP and HP structure model as the refinement fitting (green). The background is refined manually and indicated in red curves.

3. *Presence of a Pressure-Transmitting Medium*

Fig. 5 summarises the integrated diffraction patterns for $FePSe_3$ powder samples loaded in a DAC without a pressure medium. A pressure-transmitting medium is absent in this DAC. No peak broadening was observed at any pressure. A number of new peaks started to appear at 9.6 GPa marking the onset of the phase transition. We mark the pure LP phase with blue. Data above 16.3 GPa showed peaks consistent with a pure HP phase, as marked in orange. Diffraction patterns between these two pressures could be fitted with both LP and HP phases.

The systematically fitted weight factor for the two phases using `GSAS – II` [4] is provided underneath. The LP and HP coexist for a wide pressure range. With the increased pressure, the HP phase increases while the LP decreases. The relative weight factors evolve smoothly throughout this wide two-phase co-existence region.

The absence of helium as the pressure-transmitting medium raised the transition pressure for the emergence of the HP phase and also contributed to a quite wide region of coexistence.

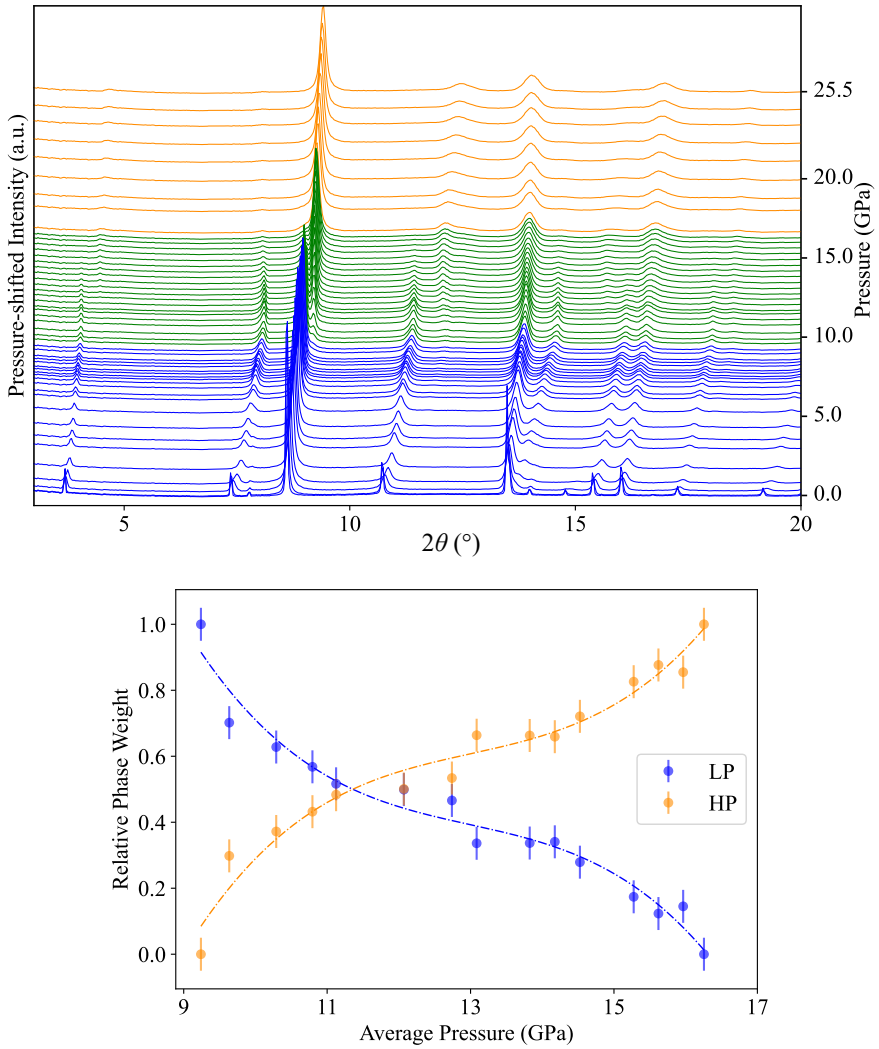

FIG. 5. Integrated diffraction patterns of $FePSe_3$ powder sample in a DAC loaded without helium as the pressure-transmitting medium at different pressure values. The intensity has been normalized to the maximum intensity at each pressure point. An offset proportional to the pressure value for each measurement has been added as well. Blue and orange represent a single phase of LP and HP while green refers to the coexistence of both phases. The relative phase weight change as a function of pressure is shown below.

D. Single Crystal Samples in DAC

1. *Lattice Parameter Direct Refinement*

A parametric refinement using CrysAlisPro of the single crystal data, starting with parameters at 0 GPa and using fits to give start parameters at higher pressure, in shown in Table I. The table summarizes the lattice parameters of $FePSe_3$ at ambient pressure known from previous literature [5] and the directly refined values from our sample at varying pressure points. It should be noted that `CrysAlisPro` only gives dimensions and angles with an error based on the indexed reflections while refining the unit cell. The directly refined lattice parameters are tolerable within a hexagonal cell's description where $a = b$, $\alpha = \beta = 90°$ and $\gamma = 120°$. Our sample at ambient pressure, measured before closing the pressure cell, matches nicely with the previously reported values. A line break is added in the table for guidance in between which pressure points the lattice parameter c collapsed abruptly.

TABLE I. Directly refined lattice parameters of single-crystal $FePSe_3$ at different pressures resulting from the synchrotron diffraction data. The ambient-pressure lattice parameters from Ref [5] are listed in the first row for comparison. We used the same hexagon cell description for refinements at all pressures.

Pressure (GPa)	a (Å)	b (Å)	c (Å)	α (°)	β (°)	γ (°)
0, Ref[5]	6.265(6)	6.265(6)	19.80(2)	90.0	90.0	120.0
0	6.205(3)	6.212(5)	19.59(3)	90.28(14)	89.90(12)	119.99(7)
1.4	6.185(4)	6.176(3)	18.89(3)	90.24(9)	90.38(13)	119.97(6)
2.5	6.144(3)	6.147(2)	18.81(3)	89.89(8)	90.01(12)	120.06(5)
4.4	6.091(3)	6.096(2)	18.34(3)	89.59(8)	90.10(10)	120.03(4)
6.7	6.044(3)	6.046(2)	18.06(3)	90.15(7)	89.96(11)	120.04(4)
7.8	6.021(2)	6.020(2)	16.48(2)	90.01(8)	90.31(7)	120.00(4)
10.0	6.0015(17)	5.9995(17)	15.96(2)	90.26(6)	89.90(6)	119.98(3)
11.8	5.9921(14)	5.9900(17)	15.74(2)	90.00(6)	90.06(5)	120.00(3)
15.6	5.9684(16)	5.9623(18)	15.61(2)	90.07(7)	90.08(6)	120.02(3)
18.1	5.9450(16)	5.9440(16)	15.34(2)	89.77(6)	89.94(6)	119.96(3)
22.0	5.916(2)	5.9327(17)	14.84(2)	89.97(6)	89.99(7)	120.05(3)
25.0	5.8972(17)	5.9145(15)	14.61(2)	89.85(6)	90.14(6)	120.03(3)
28.0	5.8925(15)	5.8988(16)	14.46(2)	89.75(6)	90.27(6)	120.18(3)

2. HP Structural Model

Friedel Pairs Analysis - Break of cetrosymmetric symmetry In centrosymmetric structure, Bragg peaks at (hkl) and $(\bar{h}\bar{k}\bar{l})$ are equivalent and expected to have the same structure factors. Such pairs are Friedel pairs. We analyzed the observed structure factor (I_{obs}) in $P1$ symmetry for the 10 GPa data across all pairs of $I(hkl)$ and $I(\bar{h}\bar{k}\bar{l})$. Fig. 6 displays the analysis graphically. The $I_{obs}(hkl)$ and $I_{obs}(\bar{h}\bar{k}\bar{l})$ plot presents clear deviation from the $y = x$ line. Additionally, we ruled out the deviation from random noise by analyzing the statistical distribution. Here we took the observed intensity difference as $\Delta I_{obs} = I_{obs}(hkl) - I_{obs}(\bar{h}\bar{k}\bar{l})$ and σ, and the standard uncertainty $\sigma(\Delta I_{obs}) = \sqrt{\sigma^2(I_{obs}(hkl)) + \sigma^2(I_{obs}(\bar{h}\bar{k}\bar{l}))}$. Then we could use the $Z_{obs} = \frac{\Delta I_{obs}}{\sigma(\Delta I_{obs})}$ to unambiguously show that our observation is a result of scattering conditions, instead of any random statistical noise during the measurements. We hence conclude that the centrosymmetric symmetry is broken in the HP phase.

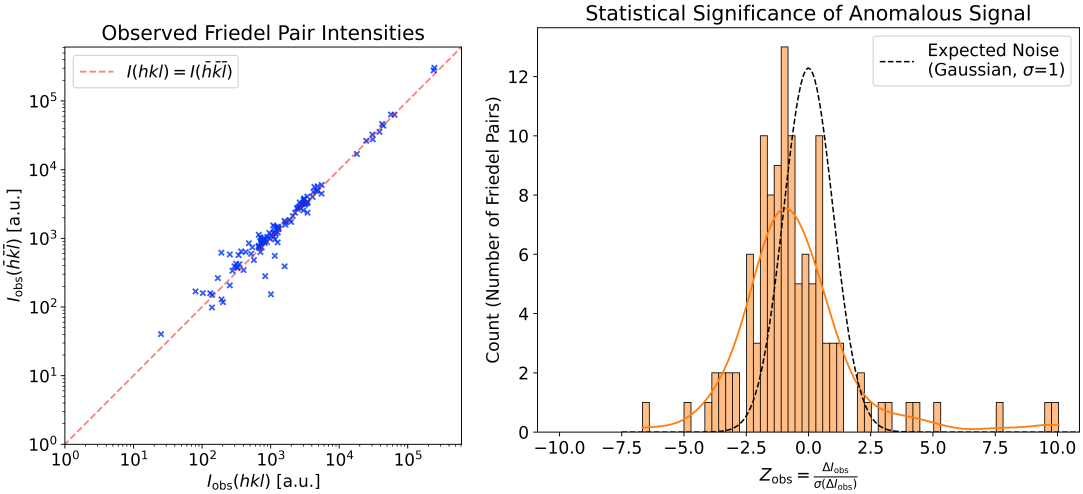

FIG. 6. (left) The direct comparison of $I(hkl)$ and $I(\bar{h}\bar{k}\bar{l})$ in reference to the $y = x$ dotted red line. (right) The statistical distribution of the $\Delta I = I(hkl) - I(\bar{h}\bar{k}\bar{l})$ for the 10 GPa HP data in $P1$ symmetry in orange histograms versus the random noise following a Gaussian-type function as expected in centrosymmetric phase.

Structure Factors Analysis We analyzed one selected set of HP data (10 GPa), using $R\bar{3}$, $R3$ and $P1$ as the structure model respectively using `CrysAlisPro`. The observed versus the calculated structure factors are shown graphically in Fig. 7. We also provide the reduced crystallographic data in the Table. The refinement parameters in $R3$ space group give the best fitting.

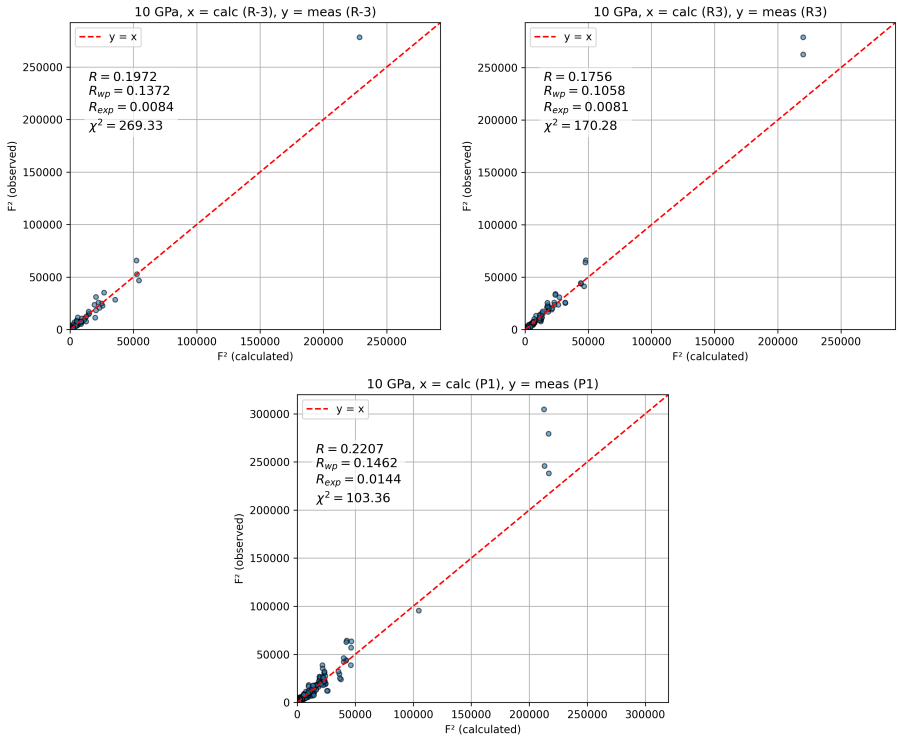

FIG. 7. The observed structure factor versus the calculated structure factor in $R\bar{3}$ and $R3$ space group, respectively, for the data collected at 10.0 GPa.

TABLE II. Reduced crystallographic data of single-crystal $FePSe_3$ at 10.0 GPa from the single-crystal X-ray diffraction experiment, using $R\bar{3}$, $R3$ and $P1$ as the structure model.

	$R\bar{3}$	$R3$	$P1$
a	6.0195(16)	6.0155 (7)	5.9698(9)
b	6.0195(16)	6.0155 (7)	5.9699(11)
c	15.46(14)	15.34 (6)	15.608(12)
α	90	90	90.10(4)
β	90	90	90.05(4)
γ	120	120	119.998(18)
Refinement parameters			
$R_1[F^2 \geq 2\sigma(F^2)]$	0.1243	0.0895	0.1303
$wR_2([F^2 \geq 2\sigma(F^2)])$	0.3106	0.2177	0.3298
$R_1(F^2)$	0.1300	0.0934	0.1657
$wR_2(F^2)$	0.3159	0.2207	0.3489
S (Goodness-of-fit on F^2)	1.231	2.097	2.439
Reflections collected	291	249	1141
Independent Reflections	79	125	782

3. Comparative Evolution of Lattice Parameters

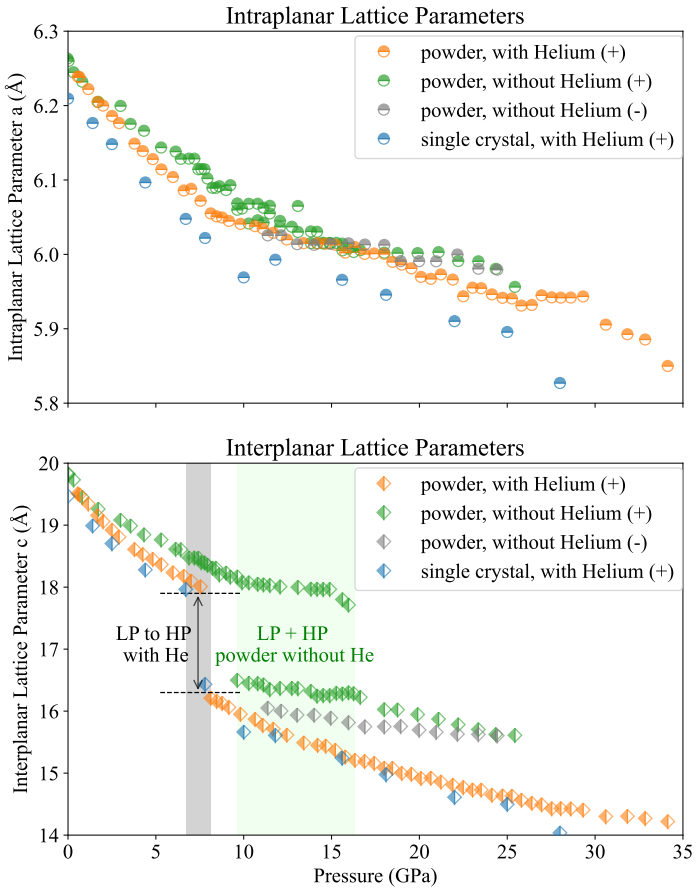

FIG. 8. The evolution of intra- and interplanar lattice parameters a and c of $FePSe_3$ with the application of pressure at different experimental scenarios. (+) represents the values fitted from the compression process while (-) represents those obtained during decompressing.

Fig. 8 summarizes how the intraplanar lattice parameter a and the interplanar c evolve in response to the applied pressure across different experimental conditions. The shaded block in grey indicates the pressure region where the c collapse occurred in the presence of helium as PTM. It can be seen that the LP to HP structural transition occurred as a first-order transition for both powder and single crystal samples at a consistent pressure around 7 GPa. In the other DAC loaded merely with powder $FePSe_3$ samples, the LP-HP transition pressure was postponed to a higher pressure value (the left edge of the green block). Additionally, there was a wide pressure range where the LP and HP phases coexist. It can be concluded that different pressure conditions can effectively affect structural evolution, with differences in the value of the transition pressure and the occurrence of phase-coexistence depending on the choice of the pressure medium.

E. LP and HP Structural Model

The data were subsequently reduced in the LP model with space group $R\bar{3}$ below 6.7 GPa and HP mode with space group $R3$ above 7.8 GPa. In correspondence to the sets of representative crystallographic data after the data reduction in the main text, here we provide the atomic position information in the following tables.

TABLE III. Wyckoff positions of $FePSe_3$ at 4.4 GPa in the $R\bar{3}$ space group.

4.4 GPa, $R\bar{3}$

Atoms	x	y	z	Wyckoff Site
Fe	$\frac{1}{3}$	$\frac{2}{3}$	0.5	$6c$
P	$\frac{1}{3}$	$\frac{2}{3}$	0.593(5)	$6c$
Se	0.659(5)	0.663(1)	0.580(5)	$18f$

TABLE IV. Wyckoff positions of $FePSe_3$ at 10.0 GPa and 28.0 GPa in the $R3$ space group.

10.0 GPa, $R3$

Atoms	x	y	z	Wyckoff Site
Fe_1	$\frac{1}{3}$	$\frac{2}{3}$	0.489(5)	$3a$
Fe_2	$\frac{2}{3}$	$\frac{1}{3}$	0.510(7)	$3a$
P_1	0	0	0.5945(13)	$3a$
P_2	0	0	0.4475(15)	$3a$
Se_1	0.6239(12)	0.0053(10)	0.5725(3)	$9b$
Se_2	0.0016(16)	0.3536(18)	0.4026(15)	$9b$

28.0 GPa, $R3$

Fe_1	$\frac{1}{3}$	$\frac{2}{3}$	0.5016(4)	$3a$
Fe_2	$\frac{2}{3}$	$\frac{1}{3}$	0.4984(7)	$3a$
P_1	0	0	0.5613(4)	$3a$
P_2	0	0	0.4217(60)	$3a$
Se_1	0.3781	0.0594	0.5830(24)	$9b$
Se_2	0.0293	0.6377	0.4057(6)	$9b$

II. NEUTRON POWDER DIFFRACTION AND MAGNETIC STRUCTURES

A. Background Subtraction

Fig. 9 presents the raw diffraction data in red scattered circles below the magnetic transition temperature for the three measured pressures. At each pressure, the broad and diffuse background was estimated by manually specifying a few background points and then fitting a smooth Chebychev polynomial through them. The fitted background is displayed in solid black lines. The blue circles present the intensity data after subtracting the background from the raw data, on the same scale as the raw data. The diamond peaks at $2\theta \sim 70°$ were cut off as they exceeded the scale.

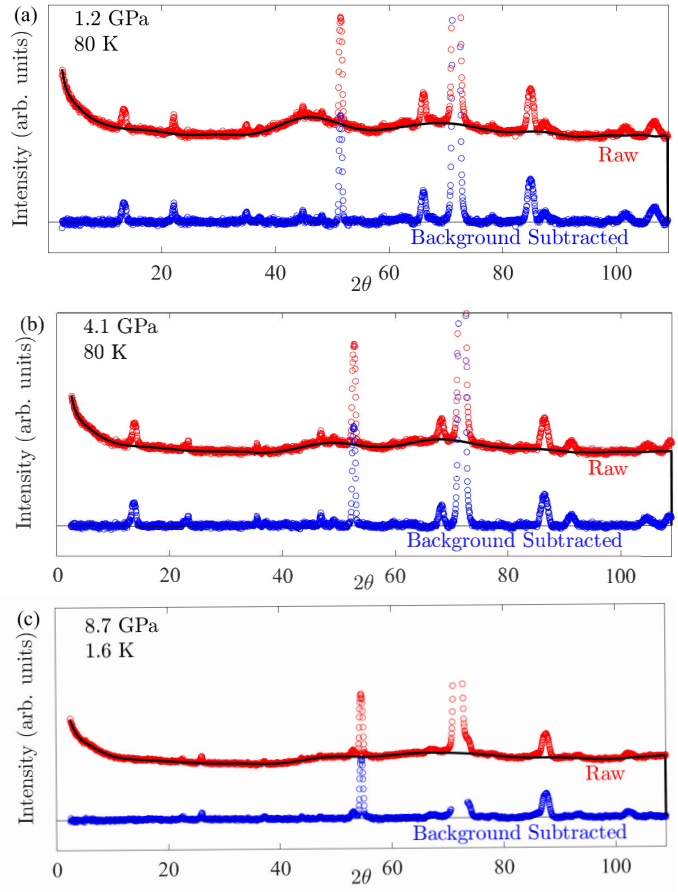

FIG. 9. The neutron diffraction intensity raw data (red) minus the fitted background curve (black) results in the intensity data (blue) for further data analysis. All three subplots are on the same scale.

B. Data Refinements and Additional Diamond Peaks

Fig. 10 shows the resulting data (red circles) after background subtraction for 1.2 GPa, 4.1 GPa and 8.3 GPa at 80 K, 80 K and 1.6 K, respectively. Extra peaks originating from the diamond anvils were seen in addition to the sample signals, being marked with green arrows. The diamond peaks were easily identified as they do not noticeably shift with pressure. There is one prominent peak at around $2\theta = 72°$ (full extent is off the scale of the presented datasets), and smaller peaks at 22° and 37° from higher harmonics of one-third the measurement wavelength $\frac{\lambda}{3}$ from the D20 monochromator. The peak at 22° coincides with sample peaks at some pressures, so had to be removed from the data before refinement and is not marked in the data shown. To do this, a Lorentzian peak shape was fitted to it at high pressure, where it was not superimposed on other features at similar 2θ, and the resulting function was subtracted from all datasets. The remaining diamond peaks were excluded from refinement.

The resulting data were then refined using the Rietveld method as implemented in software `GSAS-II` [4] and `FullProf` [6], including separate phases for the nuclear and magnetic contributions (see Table V). It was necessary to include asymmetry parameters to describe the peak shapes seen in the data, due to the extremely two-dimensional nature of the crystallites. Minor preferred orientation parameters were considered for data at 4.1 and 8.3 GPa and were kept the same through the refinements. The refinement parameters between pressures were kept as consistent as possible. The used asymmetric parameters are summarized in Table VI. All peaks were well indexed and no additional unexplained peaks were observed in the data.

TABLE V. The resulting crystallographic data and the refinement parameters from $FePSe_3$ powder neutron diffraction data at the measured pressures of 1.2 GPa, 4.1 GPa and 8.3 GPa. We use the primitive hexagon cell description for the lattice parameters.

	1.2 GPa 80 K	4.1 GPa 80 K	8.3 GPa 1.6 K
Phase	LP	LP	HP
Space group	$R\bar{3}$	$R\bar{3}$	$R3$
a (Å)	6.2237(5)	6.1187(3)	6.0778(5)
c (Å)	19.136(2)	18.268(2)	16.311(2)
Volume (Å^3)	641.83(11)	592.29(9)	521.80(9)
Magnetic moment, R_z	3.84 μ_B	3.84 μ_B	-
Propagation vector	$[\frac{1}{2}0\frac{1}{2}]$	$[\frac{1}{2}0\frac{1}{2}]$	-
Refinement Parameters			
χ^2	3.37	4.25	4.85
R	18.64%	18.49%	10.27%
wR	19.67%	22.00%	12.88%

TABLE VI. Preferred orientation and asymmetric parameters used for refinements.

Pressure (GPa)	Pref1	Pref2	Asy1	Asy2	Asy3	Asy4
1.2	0.00000	0.00000	-1.19385	-0.05863	2.81088	0.22351
4.1	0.19448	0.00000	-1.28012	-0.06923	2.95166	0.22351
8.3	0.19448	0.00000	-1.28012	-0.06923	2.95166	0.22351

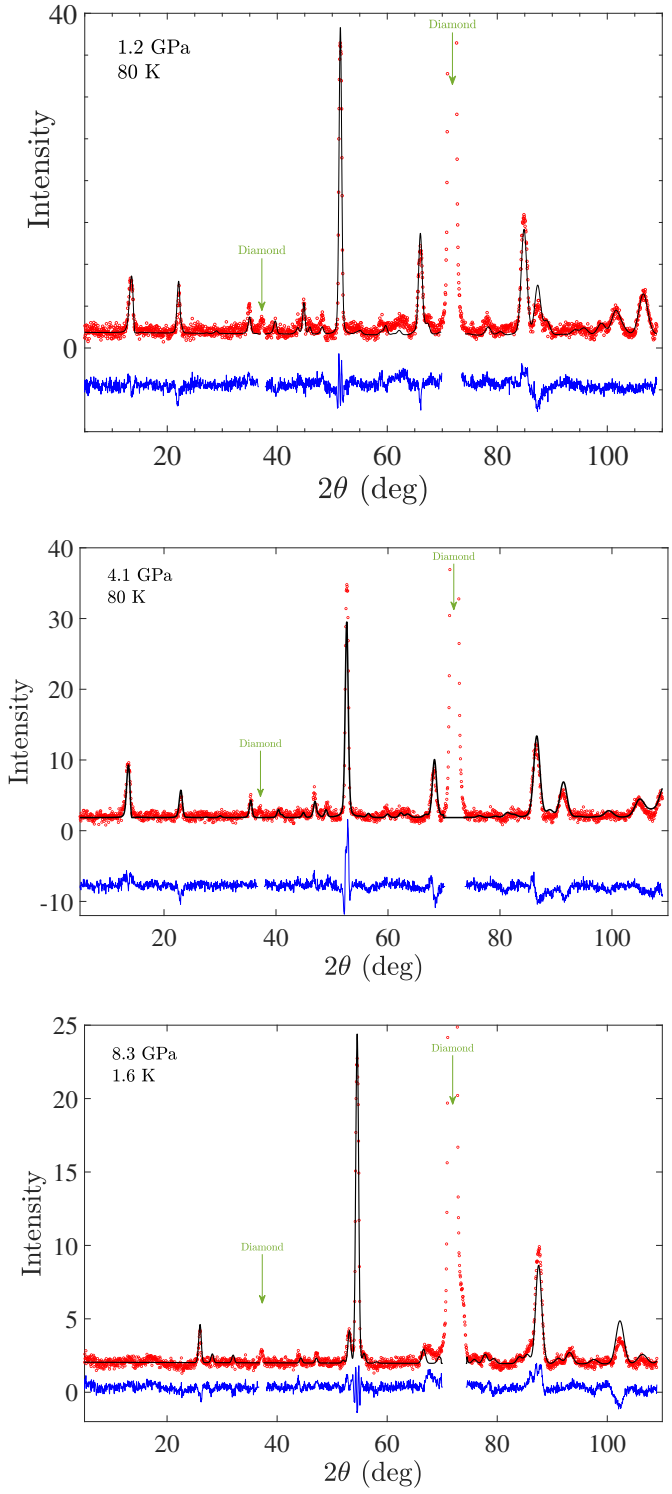

FIG. 10. Refinement of the post-processed neutron diffraction data after background subtraction for 1.2 and 4.1 GPa taken at 80 K, and 8.3 GPa taken at 1.6 K. At 8.3 GPa, the sample has now undergone its structural transition, and additionally, there are no magnetic peaks visible.

C. Estimation of Néel Transition Temperatures

Except for the key scans discussed in the main text, we also collected neutron data while warming the cell under constant load and thus pressure. A series of measuring with 15-minute counting time was conducted while heating from 80 to 250 K for 1.2 GPa, from 80 to 300 K for 4.1 GPa, and 30-minute counting time from 1.6 to 300 K for 8.3 GPa, as summarized in Table VII.

TABLE VII. Measurements while heating from low-temperature (LT) to high-temperature (HT) at different pressures for powder samples of $FePSe_3$.

Pressure (GPa)	LT → HT (K)	Counting Time (min)
1.2	80 → 245	15
4.1	80 → 300	15
8.3	1.6 → 300	30

The evolution of the magnetic peaks' intensity as a function of temperature was able to give a quantitative estimation of the Néel temperature at different pressures. At 1.2 GPa, we were able to fit the thermal variation of the integrated intensity with a honeycomb-lattice 2D Ising model [7], as expressed in Eq. 2. More details of how to apply the model can be found within a previous successful applied case in $FePS_3$ [8].

$$M = \left[1 - \frac{16z^3\left(1+z^3\right)\left(1+z^2\right)^3}{\left(1-z^2\right)^6}\right]^{1/8} \tag{2}$$

The fit gave $T_N \sim 128 \pm 10$ K and $4J \sim 19.4(6)$ K. The data points from interval scans and the fitted curve are shown in Fig. 11.

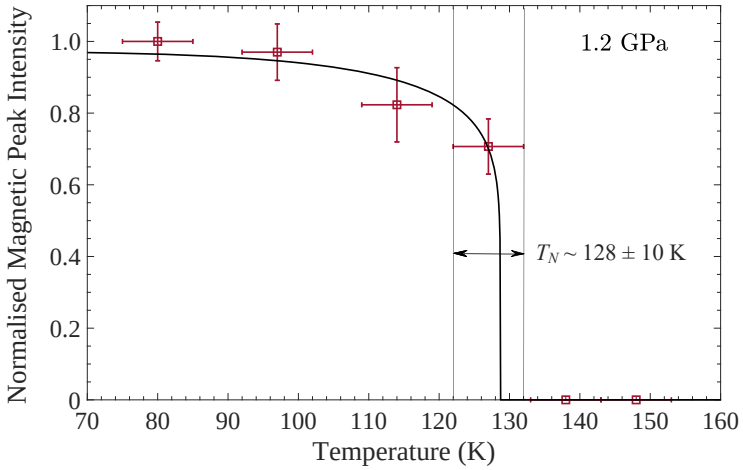

FIG. 11. Temperature dependence of integrated magnetic peak intensity at 1.2 GPa, to fit and extract the value of T_N. The data are fit to the model described in [7], which was used to describe the Ising-like response of moments in one neighboring compound $FePS_3$ [8]. The horizontal error bar corresponds to the temperature range during one measurement while heating (15-minute counting time).

III. TRANSPORT MEASUREMENTS AND ANALYSIS

A. Original Resistance Data

Fig. 12 shows the original resistance (R) data obtained while measuring two different single-crystal samples from the same batch of $FePSe_3$ in a CAC. Both samples show consistent results that $FePSe_3$ remains insulating up to 6.0 GPa and turns to conducting phase around 6.0∼8.0 GPa. We also observe hysteresis in the 6.0 GPa data for sample 2. The resistivity (ρ), shown in the main text, was calculated as described in the method section.

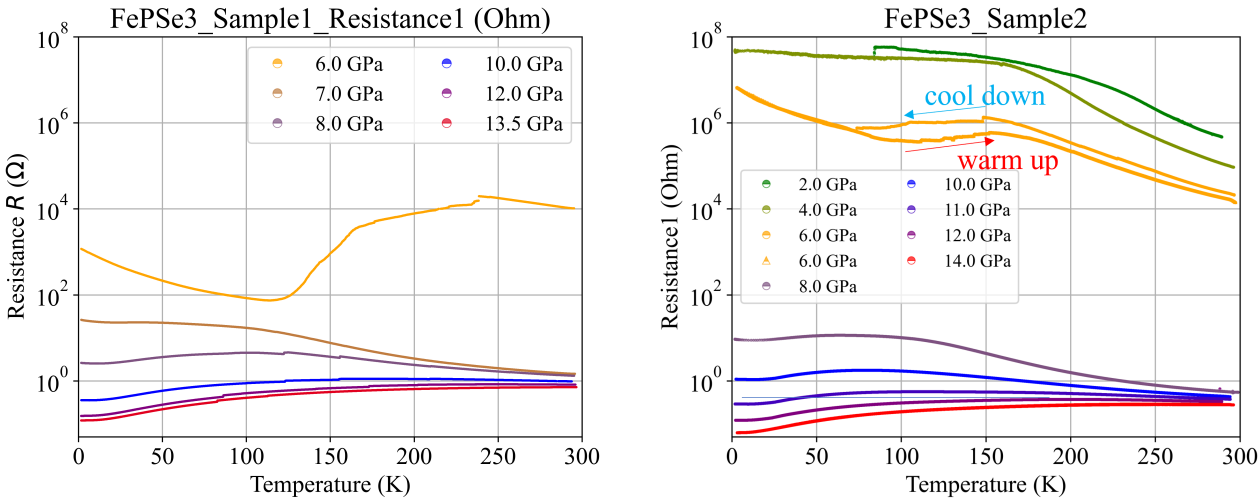

FIG. 12. The original resistance data of $FePSe_3$ at different pressures for sample 1 and sample 2.

B. The LP phase ($P \leq 6$ GPa)

1. *Thermally Active Arrhenius behavior*

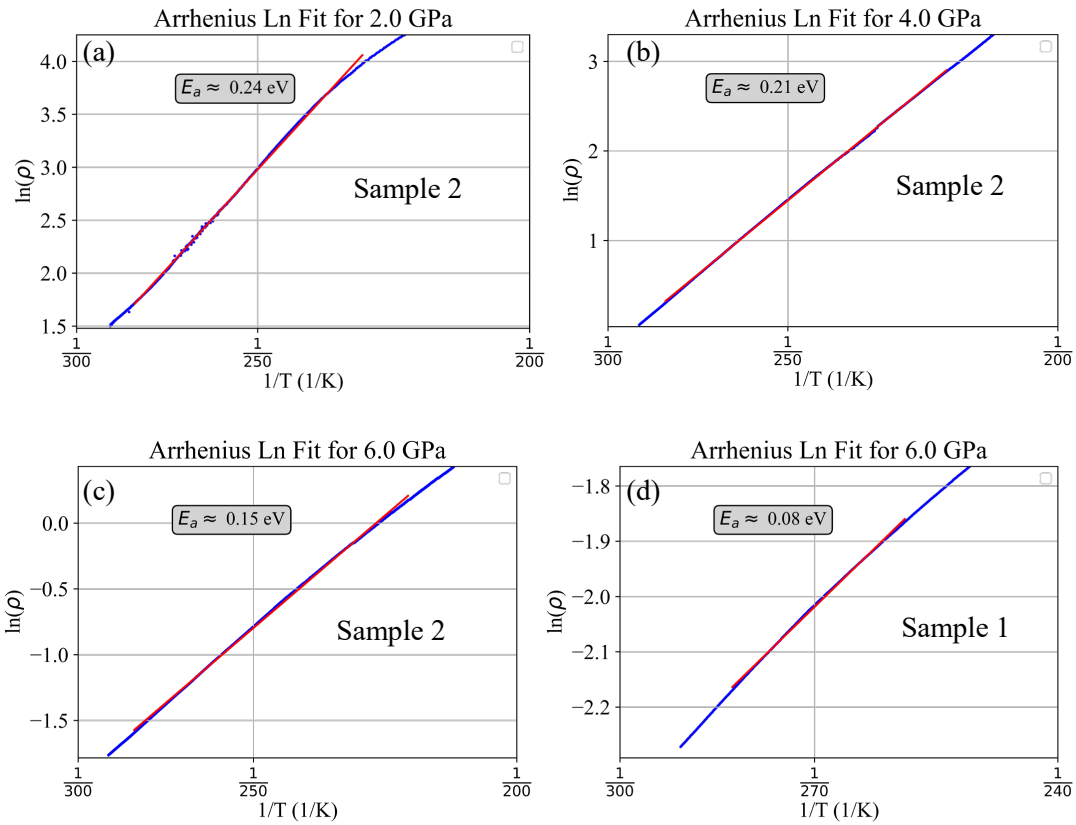

FIG. 13. Resistivity in natural logarithm $\ln(R)$ as a function of $1/T$ (blue) and the Arrhenius fit (red) for sample 2 at 2.0, 4.0 and 6.0 GPa and sample 1 at 6.0 GPa.

Below the insulator-to-metal transition pressure, $FePSe_3$ is still behaving as an insulator. We thus can analyze the activation energy E_a following the activated Arrhenius Equation,

$$\rho(T) \sim e^{E_a/(k_B T)}$$

In sample 1, we select the 300 to 250 K temperature range where the conduction is dominated by thermally activated behavior and thus can be described by a simple Arrhenius process. Fig. 13 plots the $\ln(\rho)$ as a function of $1/T$ to allow for straightforward linear fitting. A polynomial fitting is performed and indicated with the red solid line. The activation energy can thus be obtained from the slope, being around 0.08 eV. Since our $FePSe_3$ sample, only shows 1% superconducting impurity, we could relate the activation energy to the value of the band gap. The subtle deviation at the highest temperature might arise from the saturation effect of thermal carriers. Further investigations would be needed to investigate the exact mechanism of electrical conduction between valence and conduction bands.

In sample 2, we performed the analysis in the same way and obtained the fitted band gap values of 0.24, 0.21 and 0.15 eV for 2.0, 4.0 and 6.0 GPa. Pressure shrinks the insulating band gap in the insulating phase.

2. *Abnormal Change in Resistivity - Potential Magnetic Transition*

At 6 GPa in sample 1, we also observe one discernible change in the resistance-temperature curve with a broad minimum at approximately 124 K, as shown in Fig. 14. This abnormal change of resistivity could be the result of an antiferromagnetic transition with temperature. The broad peak feature potentially suggests reduced dimensionality. Further efforts, for instance, magnetic susceptibility measurements, would be needed to retrieve the full information regarding this transition.

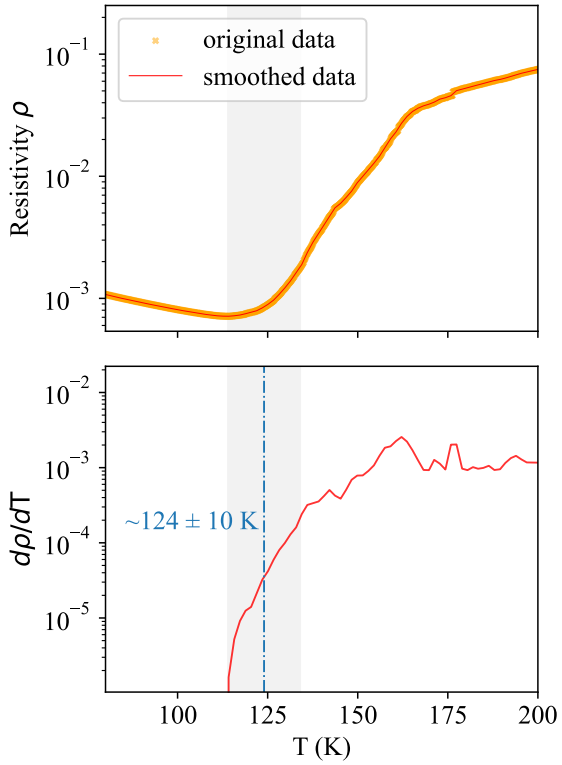

FIG. 14. A zoom-in view of resistivity (top) and the derivative of resistance $d\rho/dT$ (bottom) as a function of temperature T. The abnormal change region is marked with a color block to guide the eye.

C. The HP phase ($P > 6$ GPa)

1. T^2 Fitting below 40 K

In the metallic phase, we found that the resistivity of $FePSe_3$ at low temperatures can be welled described by

$$\rho = \rho_0 + A\ T^2$$

We plot the resistivity ρ as a function of T^2 to allow for straightforward polynomial fitting. To find the optimum temperature range, we start with a wide range of T from a minimum value T_{min} of 2 K to the maximum value T_{max} of 40 K. A linear fit $\rho \sim T^2$ was performed and the standard error was recorded. The minimum and maximum limit changes with a step size of 1 K and the standard error for each range was recorded. The minimal temperature difference between T_{max} and T_{min} is set to be 5 K. In the end, we identify the best-fitting temperature range with the smallest standard error. The results of the fitting are shown below.

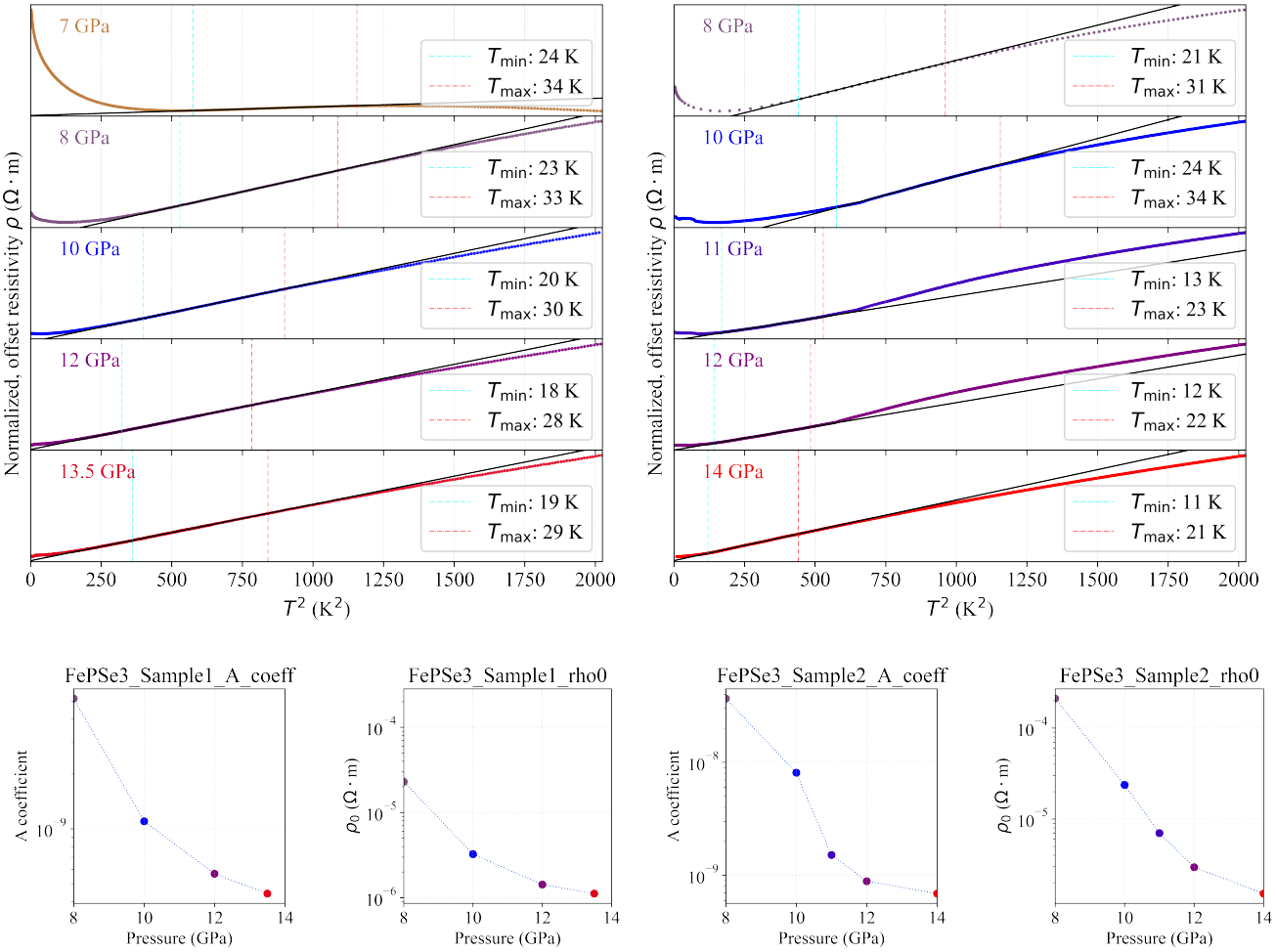

FIG. 15. The T^2 linear fit for resistivity in the metallic phase for sample 1 (left) and sample 2 (right).

2. *Absence of SC and Resistivity Drop below 10 K*

We did not observe superconductivity in two sets of independent measurements. The cubic anvil cell provided highly hydrostatic pressure conditions, and measurement currents were kept low ($< 10\ \mu$A), thus ruling out the most common extrinsic reasons for not observing a superconducting phase. Yet we did observe a small ($\sim$1% of $\rho(T \to 0)$) decrease in the resistivity around 3 K at 10.0 GPa which rises to around 4 K at 13.5 GPa only in one of the samples being measured, as shown in Fig. 16.

We do not have an immediate explanation for the contradiction but note that elemental Se [9, 10], Fe [11] and FeSe [12] have been reported to turn SC at coincidentally comparable values to those reported by Wang *et al.*.

Additionally, we recognize that SC has been reported in many other $TMPX_3$ compounds, including $NiPSe_3$ [13], $SnPS_3$ [14], $SnPSe_3$ [15], $CrSbSe_3$ [16] and the medium-entropy compounds [17]. But SC has not been reported so far in $FePS_3$, for instance.

One should note that measuring high-resolution resistivity data in single-crystal van der Waals compounds is not an easy task. A critical premise lies in high-quality crystals and a clear understanding of the high-pressure structures.

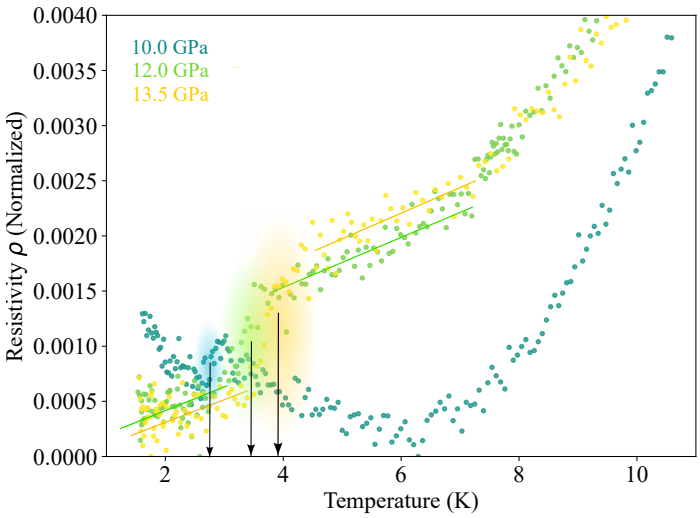

FIG. 16. A zoom-in normalized resistivity at 10.0, 12.0, and 13.5 GPa. The resistivity drop is shown by shaded regions with black arrows to guide the eye.

[1] H. K. Mao, J. Xu, and P. M. Bell, Calibration of the ruby pressure gauge to 800 kbar under quasi-hydrostatic conditions, J. Geophys. **91**, 4673 (1986).

[2] G. Shen, Y. Wang, A. Dewaele, C. Wu, D. E. Fratanduono, J. Eggert, S. Klotz, K. F. Dziubek, P. Loubeyre, O. V. Fatyanov, P. D. Asimow, T. Mashimo, and R. M. M. Wentzcovitch, Toward an international practical pressure scale: A proposal for an IPPS ruby gauge (IPPS-Ruby2020), High Press. Res. **40**, 299 (2020).

[3] J. Filik, A. Ashton, P. Chang, P. Chater, S. Day, M. Drakopoulos, M. Gerring, M. Hart, O. Magdysyuk, S. Michalik, et al., Processing two-dimensional X-ray diffraction and small-angle scattering data in DAWN 2, J. Appl. Cryst. **50**, 959 (2017).

[4] B. H. Toby and R. B. Von Dreele, GSAS-II: the genesis of a modern open-source all purpose crystallography software package, J. Appl. Cryst. **46**, 544 (2013).

[5] R. Brec, D. M. Schleich, G. Ouvrard, A. Louisy, and J. Rouxel, Physical properties of lithium intercalation compounds of the layered transition-metal chalcogenophosphites, Inorg. Chem. **18**, 1814 (1979).

[6] J. Rodríguez-Carvajal, Fullprof, CEA/Saclay, France **1045**, 132 (2001).

[7] R. J. Baxter, Exactly solved models in statistical mechanics (Courier Corporation, 2007).

[8] K. C. Rule, G. J. McIntyre, S. J. Kennedy, and T. J. Hicks, Single-crystal and powder neutron diffraction experiments on $FePS_3$: Search for the magnetic structure, Phys. Rev. B **76**, 134402 (2007).

[9] F. P. Bundy and K. J. Dunn, Electrical behavior of te, se, and s at very high pressures and low temperatures: Superconduction transitions, Phys. Rev. B **22**, 3157 (1980).

[10] Y. Akahama, M. Kobayashi, and H. Kawamura, Pressure-induced superconductivity and phase transition in selenium and tellurium, Solid state communications **84**, 803 (1992).

[11] K. Shimizu, T. Kimura, S. Furomoto, K. Takeda, K. Kontani, Y. Onuki, and K. Amaya, Superconductivity in the non-magnetic state of iron under pressure, Nature **412**, 316 (2001).
[12] F.-C. Hsu, J.-Y. Luo, K.-W. Yeh, T.-K. Chen, T.-W. Huang, P. M. Wu, Y.-C. Lee, Y.-L. Huang, Y.-Y. Chu, D.-C. Yan, et al., Superconductivity in the PbO-type structure α-FeSe, Proc. Natl. Acad. Sci. **105**, 14262 (2008).
[13] H. Sun, L. Qiu, Y.Han, E. Yi, J. Li, M. Huo, C. Huang, H. Liu, M. Li, W. Wang, D. Yao, B. A. Frandsen, B. Shen, Y. Hou, and M. Wang, Coexistence of zigzag antiferromagnetic order and superconductivity in compressed $NiPSe_3$, Mater. Today Phys. **36**, 101188 (2023).
[14] B. Yue, W. Zhong, T. Wen, Y. Wang, H. Yu, X. Yu, C. Chen, J.-T. Wang, and F. Hong, Pressure-induced ferroelectric-to-superconductor transition in $SnPS_3$, Phys. Rev. B **107**, L140501 (2023).
[15] M. Qi, W. Chen, Y. Huang, H. Song, X. Lv, M. Wu, W. Zhao, L. Zhang, and T. Cui, Pressure-induced superconductivity in van der waals layered semiconductor $snpse_3$, J. Mater. Chem. C. **12**, 5108 (2024).
[16] C. Li, Y. Wang, K. Liu, D. Jiang, J. Feng, T. Wen, B. Yue, Y. Zhou, L. Sun, and Y. Wang, Superconductivity in Quasi-One-Dimensional Ferromagnet $CrSbSe_3$ under High Pressure, J. Am. Chem. Soc. **146**, 9688 (2024).
[17] X. Chen, J. Wang, T. Ying, D. Huang, H. Gou, Q. Zhang, Y. Li, H. Hosono, J. Guo, and X. Chen, Insulator-metal-superconductor transition in the medium-entropy van der Waals compound $M\mathrm{PSe}_3$ (M = Fe, Mn, Cd, and In) under high pressure, Phys. Rev. B **106**, 184502 (2022).